Observation of fast and slow interatomic Coulombic decay in argon dimers induced by electron-impact ionization

Xueguang Ren,[1] Tsveta Miteva,[2,3] Přemysl Kolorenč,[4] Kirill Gokhberg,[2] Alexander I. Kuleff,[2] Lorenz S. Cederbaum,[2] and Alexander Dorn[1]

[1]*Max-Planck-Institut für Kernphysik, 69117 Heidelberg, Germany*

[2]*Theoretische Chemie, Physikalisch-Chemisches Institut, Universität Heidelberg, Im Neuenheimer Feld 229, 69120 Heidelberg, Germany*

[3]*UMR 7614, Laboratoire de Chimie Physique Matière et Rayonnement, Sorbonne Universités, UPMC University Paris 06, F-75005 Paris, France*

[4]*Charles University, Faculty of Mathematics and Physics, Institute of Theoretical Physics, V Holešovičkách 2, 180 00 Prague, Czech Republic*

(Received 23 June 2017; published 20 September 2017)

We investigate the interatomic Coulombic decay (ICD) in argon dimers induced by electron-impact ionization ($E_0 = 90$ eV) using a multiparticle coincidence experiment in which the momentum vectors and, consequently, the kinetic energies for electrons and fragment ions are determined. The signature of the ICD process is obtained from a correlation map between ejected electron energy and kinetic energy release (KER) for $Ar^+ + Ar^+$ fragment ions where low-energy ICD electrons can be identified. Furthermore, two types of ICD processes, termed fast and slow interatomic decay, are separated by the ICD initial-state energies and projectile energy losses. The dependence of the energies of emitted low-energy ICD electrons on the initial-state energy is studied. ICD electron energy spectra and KER spectra are obtained separately for fast and slow decay processes where the KER spectra for the slow decay channel are strongly influenced by nuclear motion. The KER and ICD electron energy spectra are well reproduced by *ab initio* calculations.

DOI: 10.1103/PhysRevA.96.032715

I. INTRODUCTION

Electron-collision-induced processes are of great importance in a variety of applications [1], including plasma physics, astrophysics, atmospheric science, and more recently medical radiation therapy, in which the secondary low-energy electrons produced by primary ionizing radiation can lead to significant damages to biological tissue [2–4].

In weakly bound systems, e.g., in van der Waals clusters, due to the presence of the neighboring atoms, new electronic decay channels such as interatomic Coulombic decay (ICD) can be opened [5]. Here, internal excitation energy of one electronically excited constituent is transferred to a neighbor, ionizing it, which results in a low-energy electron and a pair of energetic ions. Studies of ICD have attracted a great deal of attention because of its potential role as an efficient source of low-energy electrons. The first successful experiments on ICD have been performed using photoionization of neon clusters [6] and neon dimers [7]. Since then, extensive studies of ICD in van der Waals clusters and hydrogen bonded systems have been carried out by photoabsorption experiments (see, e.g., Refs. [8–20]). Experiments of ICD induced by energetic particles like ions and electrons have also been performed mostly in rare gas dimers [21–26].

For the argon dimer (Ar_2), two different interatomic relaxation mechanisms, ICD and radiative charge transfer (RCT), have been identified in recent electron-impact [26] and photoabsorption [20] experiments in which the kinetic energies of all the final-state electrons and ions were measured in coincidence. Both ICD and RCT channels can end up in the repulsive $Ar^+ + Ar^+$ fragmentation channel. In RCT, as shown schematically by the potential energy curve diagram in Fig. 1(a), an argon atom, which is doubly ionized by electron impact, receives an electron from a neutral neighbor and emits a photon (see also Ref. [27]). The rate of this radiative charge transfer process is rather low at the equilibrium internuclear distance (R_{eq}) but is strongly increasing for decreasing R. As a result, nuclear motion in the intermediate state is enabled and the transition preferentially takes place at shorter R.

A recent *ab initio* calculation by Miteva *et al.* [28] has predicted two types of ICD channels in Ar_2, referred to as fast and slow ICD, where nuclear dynamics are strongly involved in the slow ICD process. These are shown schematically in Figs. 1(b) and 1(c), respectively, and will be discussed below in detail. The recent photoabsorption experiment in Ar_2 by Rist *et al.* examined and confirmed the effect of nuclear dynamics on ICD for the single Ar-$Ar^{+*}[3p^{-2}(^1D)4d\ ^2S]$ initial state [20].

In the present work, we aim to identify the fast and slow ICD process in Ar_2 induced by electron-impact ionization. The ICD electron energy and the kinetic energy release (KER) for $Ar^+ + Ar^+$ fragment ions are measured in the experiment. From the measurements, we determine the ICD initial state energies and analyze the projectile energy loss spectra, which allow us to identify the fast and slow ICD channels in Ar_2 and thus to study in detail the effect of nuclear dynamics on ICD. *Ab initio* calculations for the fast ICD channel are compared with the experimental data. Our experiments were carried out at the projectile energy of 90 eV, which is close to the mean energy for secondary electrons produced by ionizing radiation, e.g., in water [2]. Thus, in general the present experiment can simulate the subsequent effects of secondary electrons in weakly bonded condensed systems.

II. EXPERIMENTAL METHOD

The experiment was performed using a reaction microscope specially designed to perform electron collision experiments [30,31]. Details of the experimental setup were described

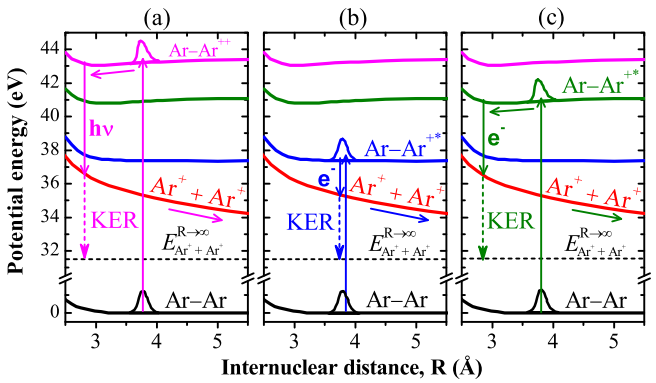

FIG. 1. Illustration of RCT (a), fast ICD (b), and slow ICD (c) processes in collisions between electrons and argon dimer. The potential energy curves were adapted from Refs. [28,29].

before [26]. Briefly, a pulsed electron beam is crossed with an argon gas jet produced by supersonic expansion. The gas jet consists of ∼98% Ar, ∼1.5% Ar_2 and ∼0.5% Ar_n ($n \geqslant 3$). The pulsed electron beam is emitted from an electron gun consisting of a tantalum photocathode, which is irradiated by a pulsed ultraviolet laser beam ($\lambda = 266$ nm, $\Delta t < 0.5$ ns). Charged collisional products (electrons as well as ions) are extracted by means of a homogeneous electric field (0.9 V/cm) and magnetic field (6.9 Gauss) and projected onto two position- and time-sensitive multihit detectors. The electron detector is centered on the projectile beam axis about 30 cm behind the target jet.

The solid angle of acceptance for detection of electrons from 2 eV up to the energy of 15 eV is almost 4π. For energies below 2 eV, and for higher energies small forward and backwards angles, are excluded due to the presence of a primary beam dump in the center of the electron detector. Above 15 eV, the angular acceptance is gradually decreasing until at ∼60 eV all electrons emitted transversally or backwards with respect to the projectile beam direction do not reach the electron detector anymore. On the other hand, the fast projectiles are predominantly scattered to forward directions and in the present experiment they are detected within a range of scattering angles between $\theta = 2^\circ$ and 20°. Therefore, projectile energy loss spectra can be easily recorded. In other cases, we compare electron spectra for monomers and dimers, which are obtained in the same experimental run and with identical detection efficiency. As a result, the finite angular acceptance does not affect the conclusions drawn from the data obtained in this work.

Experimental data for argon dimers were obtained using an electron-ion-ion triple-coincidence method where one of the final-state electrons is detected in coincidence with two Ar^+ ions. For comparison, ionization of the argon monomers was measured simultaneously using the electron-ion double-coincidence method. The momentum vectors of the emitted electrons and ions are determined from the impact positions on the detectors and the corresponding times of flight. Ions originating from a Coulomb explosion have rather high momenta which require high electric fields for efficient detection. Therefore, after 400 ns, when the electrons have reached the detector, the electric field is ramped up to 20 V/cm for extraction of the ions. An important step in the offline data analysis is to separate dimer reactions from random Ar^+/Ar^+ coincidences and from contributions of larger clusters. Therefore, dimer Coulomb explosions are identified by two energetic Ar^+ ions with equal but opposite momenta such that their sum momentum is close to zero and their sum kinetic energy is clearly beyond thermal energies in the few eV range. Larger clusters undergoing Coulomb explosion partially dissociate into ion pairs with a heavier ion like $Ar_2^+ + Ar^+$, which can be easily separated. Most others dissociating into two Ar^+ ions and neutrals can be identified if some momentum is carried by the undetected neutrals and, thus, the ions do not show the required momentum sum close to zero. Nevertheless, it is not possible to completely exclude such events in case the neutrals do not obtain significant momentum.

III. RESULTS AND DISCUSSION

In the measurements, we obtain the kinetic energies for final-state electrons and ions from the ICD and RCT reactions in Ar_2 as presented in Fig. 1 and also in Eqs. (1) and (2):

$$\begin{aligned} e^- + \mathrm{Ar}_2 \;&\rightarrow\; \mathrm{Ar} - \mathrm{Ar}^{+*}(3p^{-2}nl) + 2e^- \\ &\xrightarrow{\text{ICD}}\; \mathrm{Ar}^+ + \mathrm{Ar}^+ + e_{\text{ICD}} + 2e^- \end{aligned} \tag{1}$$

$$\begin{aligned} e^- + \mathrm{Ar}_2 \;&\rightarrow\; \mathrm{Ar} - \mathrm{Ar}^{++}(3p^{-2}) + 3e^- \\ &\xrightarrow{\text{RCT}}\; \mathrm{Ar}^+ + \mathrm{Ar}^+ + h\nu + 3e^-. \end{aligned} \tag{2}$$

Figure 2(b) shows the correlation diagram between the kinetic energy of one emitted electron and the KER for a pair of Ar^+ ions detected in coincidence. The electron spectrum includes scattered projectiles, directly ionized electrons, and low-energy ICD electrons (<10 eV), as described in Eqs. (1) and (2).

The total KER spectrum is presented in Fig. 2(a), where the emitted electron energy is integrated from 0 to 60 eV. It shows a double-peak structure in which the peak at 3.8 eV is mainly attributed to the fast ICD channel while the slow ICD and RCT channels contribute predominantly to the peak at 5.2 eV. As seen in Figs. 1(b) and 1(c) and Eq. (1), ICD in Ar_2 relies on the population of satellite states $Ar^{+*}(3p^{-2}nl)$. In the fast ICD channel, the dimer is excited to the lower-lying Ar-Ar^{+*} states with ICD lifetimes shorter than the corresponding vibrational periods [28]. Consequently, nuclear motion is negligible and the system quickly decays at R_{eq} which produces the lower KER peak at about 3.8 eV. For the slow ICD channel, the system is excited to the higher lying Ar-Ar^{+*} states with ICD lifetimes longer than the vibrational periods. Nuclear motion can take place, resulting in ICD preferentially occurring at shorter R and forming the KER peak at about 5.2 eV.

In Fig. 2(b), the faster electrons (>30 eV) are generally identified with the scattered projectiles. One can determine the projectile energy loss (E_{loss}) by the incident electron energy (E_0) minus the energy of the scattered projectile. Figure 2(c) shows the E_{loss} spectra for the $Ar^+ + Ar^+$ channels at different KER regions. Also included in Fig. 2(c) is the spectrum for the Ar^{++} dication due to the double ionization of Ar monomers. Here, the obtained minimum E_{loss} of about 43.5 eV for Ar^{++} is consistent with the lowest double ionization energy (DIE) of

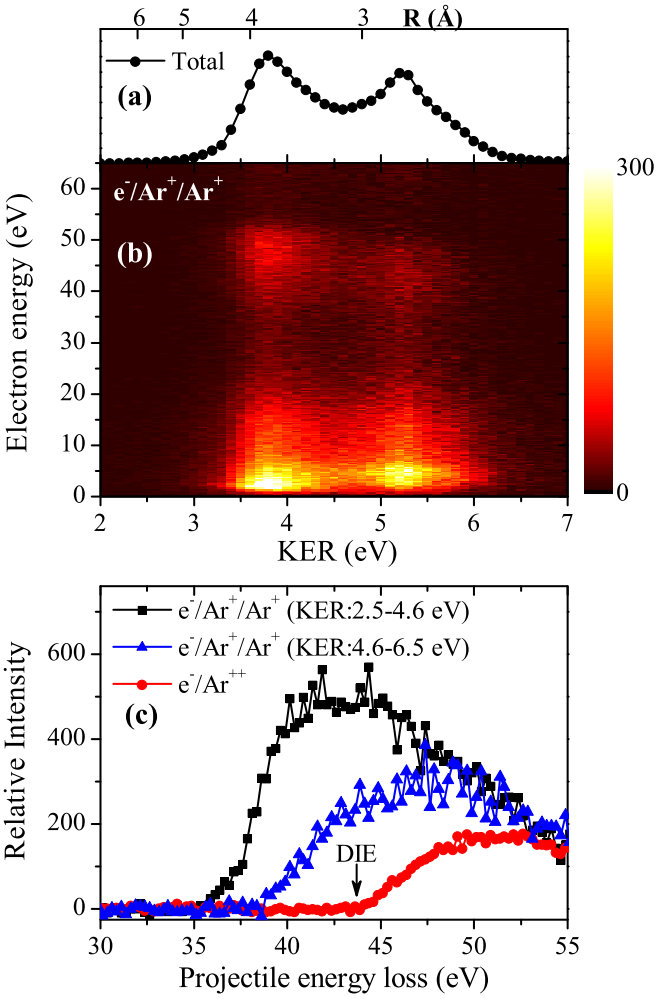

FIG. 2. (a) Total KER distribution for $Ar^+ + Ar^+$ fragment ions. (b) Measured correlation map between emitted electron energy and KER. (c) Projectile energy loss spectra for the double ionization of Ar monomer (Ar^{++}) and for the $Ar^+ + Ar^+$ fragmentation channels of Ar_2 at different KER regions.

the Ar monomer. For Ar_2, the E_{loss} of about 35.6 and 38.8 eV are obtained for the lower KER (2.5–4.6 eV) and higher KER (4.6–6.5 eV) decay channels, respectively. This demonstrates that populating lower satellites does not contribute to the high KER peak.

The emitted slow electrons (<30 eV) in Fig. 2(b) originate from both the direct ionization in the collision and the ICD processes. ICD in rare gas dimers usually manifests itself through the energy correlation between the ICD electron and the fragment ions. Such a correlation diagonal is not clearly observable in Fig. 2(b) since it contains strong background from slow electrons produced in the direct ionization process. In order to reveal the ICD signature, we subtract the directly ionized electron signal. It is obtained from the measurement of ionized electron energy spectrum of Ar monomers which is simultaneously recorded with Ar_2. Since ICD is absent for monomers, it can be considered as a reference to determine the continuous electron energy distribution due to the ejection of bound electrons from the target induced by direct electron-impact ionization.

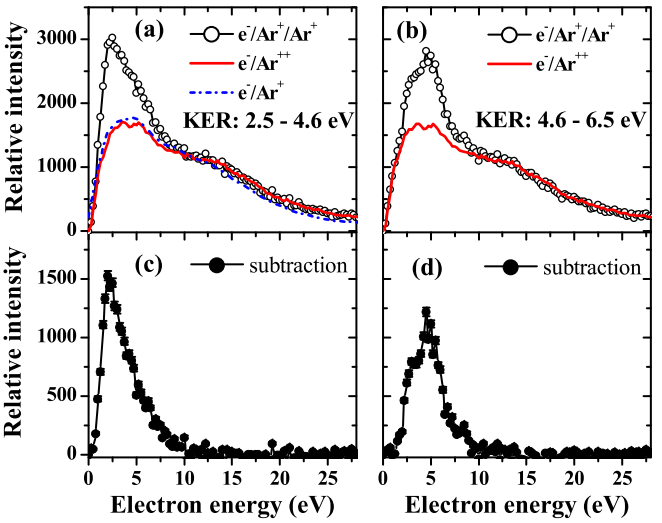

FIG. 3. Top row: the ionized electron energy spectra for Ar monomer and dimer measured in e^-/Ar^+ (dash-dotted line) and e^-/Ar^{++} (solid line) double coincidence for monomer and in $e^-/Ar^+/Ar^+$ triple-coincidence (open circles) for dimer. All spectra for monomers and dimers were normalized to each other in the energy range from 12 to 25 eV. Bottom row: the background-subtracted spectra obtained by subtracting the spectra of Ar (e^-/Ar^{++}) from Ar_2 ($e^-/Ar^+/Ar^+$). The data are summed over the KER range from 2.5 to 4.6 eV (left column) and from 4.6 to 6.5 eV (right column).

The emitted electron energy spectra for Ar monomers and dimers are presented in Fig. 3, where the results for Ar_2 are integrated over the KER range from 2.5 to 4.6 eV (fast ICD) for Fig. 3(a) and from 4.6 to 6.5 eV (slow ICD) for Fig. 3(b). Additionally, in Fig. 3(a) the spectra for Ar monomers are presented both for single ionization (e^-/Ar^+) and for double ionization (e^-/Ar^{++}). It can be seen that the shapes of the ionized slow electron energy distributions (<30 eV) are quite similar between Ar^+ and Ar^{++} in the present experiment. A closer examination shows that the electron energy distribution for dimers in the higher energy region (>15 eV) is better represented by the monomer double ionization spectrum (e^-/Ar^{++}). Therefore, we consider the electron energy spectrum for Ar^{++} as a reference to subtract the slow electron contributions due to direct ionization. The spectra for Ar monomers and dimers are normalized to each other in the energy range from 12 to 25 eV where the ICD process does not contribute [20,26,28]. As can be clearly seen in the background-subtracted electron energy spectra in Figs. 3(c) and 3(d) for dimers ($e^-/Ar^+/Ar^+$) the low-energy electron production (<10 eV) is enhanced due to the presence of the ICD processes.

Since the RCT process relies on double ionization of one atom in a dimer [see Fig. 1(a)] the number of emitted electrons and the electron energy spectrum is essentially identical as for double ionization of Ar monomers. The subtraction procedure removes not only the background of directly ionized slow electrons from single ionization but also from double ionization, and as result no signature of the RCT process is left. Thus, after subtracting the properly scaled monomer spectrum from the total electron energy spectrum of Ar_2 in Fig. 2(b), the pure ICD electron spectrum is obtained and presented

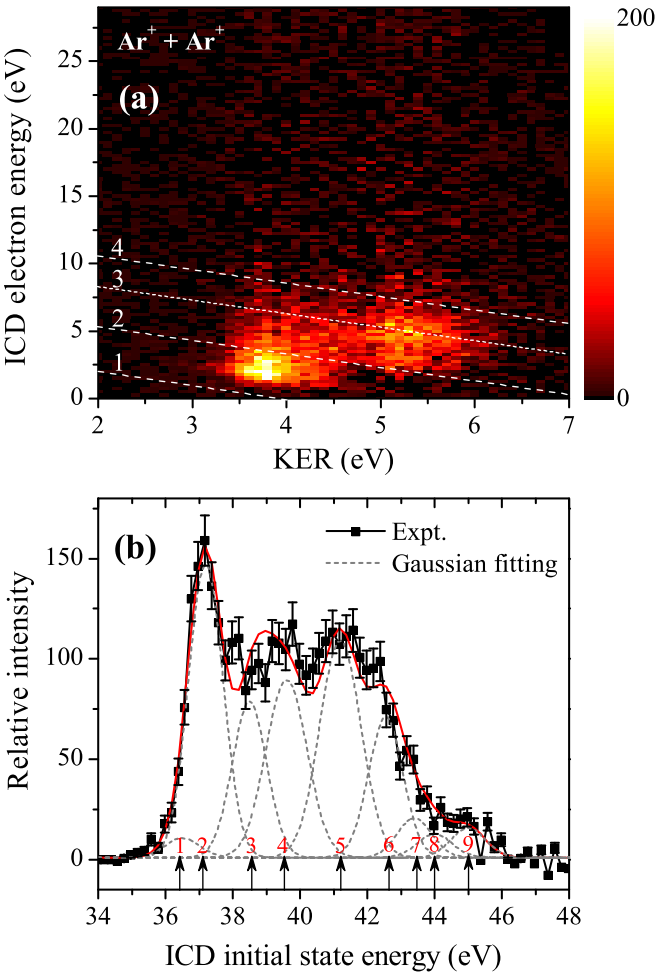

FIG. 4. (a) Correlation map between ICD electron energy and KER; (b) measured ICD initial state energy spectrum. The dashed lines are fitted Gaussian peaks corresponding to different states and the solid lines are the sum of the fits.

in Fig. 4(a) as a correlation diagram between ICD electron energy (E_{ICD}) and KER. The ICD initial state energy ($E_{\mathrm{ICD}}^{\mathrm{ini}}$), as visible from Fig. 1(b), can be determined from the measured ICD electron energy and KER as $E_{\mathrm{ICD}}^{\mathrm{ini}} = E_{\mathrm{Ar^+ + Ar^+}}^{R\to\infty} + E_{\mathrm{ICD}}$ + KER. Here $E_{\mathrm{Ar^+ + Ar^+}}^{R\to\infty} = 31.5\,\mathrm{eV}$ corresponds to the energy of the $\mathrm{Ar^+ + Ar^+}$ state at R close to infinity [26], i.e., two times the Ar ionization energy. Figure 4(b) shows the measured $E_{\mathrm{ICD}}^{\mathrm{ini}}$ spectrum, which is analyzed with a multipeak Gaussian fitting procedure. The widths of Gaussian functions are determined from the experimental resolution (≈1.2 eV), which is obtained by a calibration measurement for Ar monomer single ionization. The peak positions are obtained from the high-resolution literature values of the satellite states energies of Ar measured by electron-impact ($E_0 = 500\,\mathrm{eV}$) [32] and photoabsorption ($h\nu = 82\,\mathrm{eV}$) [33] experiments. The peak intensities are free fitting parameters. A total of nine peaks are obtained in Fig. 4(b). The assignment of the lines and the relative intensities are listed in Table I.

Furthermore, the fast and slow interatomic decay processes can be identified by the measurements of the $E_{\mathrm{ICD}}^{\mathrm{ini}}$ and the

TABLE I. ICD initial state intensities of Ar-Ar$^{+*}(3p^{-2}nl)$ extracted from Fig. 4(b).

Peak	Measured $E_{\mathrm{ICD}}^{\mathrm{ini}}$ (eV)	Intensity	State assignment
1	36.5	1.0	$3p^{-2}(^1S)4s\ ^2D$
2	37.2	15.0	$3p^{-2}(^1D)4p\ ^2P$
			$3p^{-2}(^1D)3d\ ^2D$
3	38.6	8.0	$3p^{-2}(^1D)3d\ ^2S$
4	39.6	9.0	$3p^{-2}(^1S)4p\ ^2P$
			$3p^{-2}(^3P)4d\ ^2D$
5	41.2	11.0	$3p^{-2}(^1D)4d\ ^2S$
6	42.6	7.2	$3p^{-2}(^1D)5d\ ^2S$
7	43.4	2.0	$3p^{-2}(^1D)6d\ ^2S$
8	44.0	1.2	$3p^{-2}(^1D)7d, 8d\ ^2S$
9	45.0	1.5	Rydberg series

E_{loss} of ICD in Ar_2. As shown in Fig. 2(c), the minimum E_{loss} of 35.6 and 38.8 eV are obtained for KER ∼3.8 and ∼5.2 eV channels, respectively. This means that we could extract the fast ICD channel (KER ∼3.8 eV) by selecting an energy region of ICD initial state $E_{\mathrm{ICD}}^{\mathrm{ini}}$ from 35.6 to 38.8 eV, i.e., between the two diagonal lines of (1) and (2) in Fig. 4(a). This belongs to the lower lying satellite states and corresponds to peaks 1–3 in Fig. 4(b) and Table I. In order to separate the slow decay channel, an energy region of 38.8 eV $< E_{\mathrm{ICD}}^{\mathrm{ini}} <$ 45 eV is selected, i.e., the region between the two diagonal lines of (2) and (4) in Fig. 4(a), which corresponds to the higher lying satellite states. The different KER and ICD electron energy spectra for the fast and slow decay processes are obtained and presented in Fig. 5.

As can be seen in Fig. 5(a) for the fast decay channel, the resulting KER spectrum shows essentially a single peak

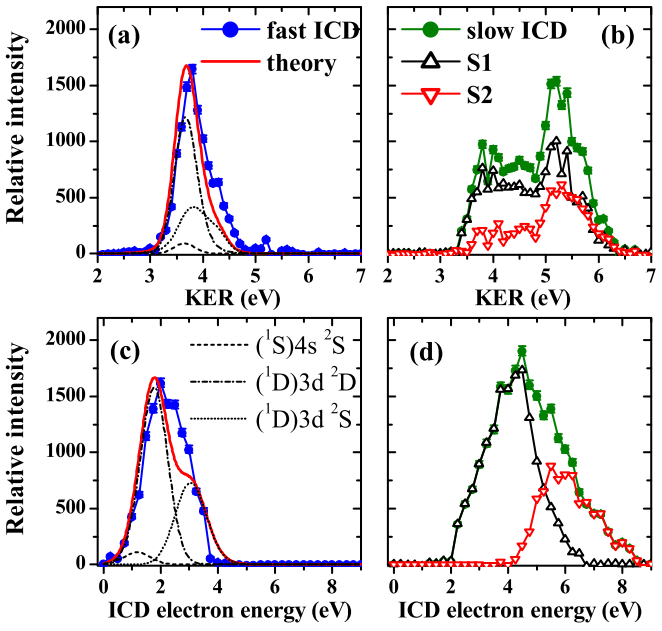

FIG. 5. Measured KER (top row) and ICD electron energy (bottom row) spectra for the separate fast (left column) and slow ICD (right column) processes. The curves are *ab initio* calculations for the fast ICD processes.

at 3.8 eV. The KER spectrum contains information about the internuclear distances at which ICD takes place and is, therefore, sensitive to the ratio of the electronic decay lifetime to the vibrational period. The peak at KER = 3.8 eV corresponds to the fast decay at R being close to R_{eq} (3.8 Å) with negligible nuclear motion. The measured electron energy spectrum for the fast ICD channel is presented in Fig. 5 (c) which shows a peak at $E_{ICD} \sim 2$ eV. The obtained KER and ICD electron energy spectra for the fast ICD processes are compared with the results of *ab initio* calculations by Miteva *et al.* [28]. The calculated KER and ICD electron energy spectra for the $(^1S)4s\ ^2S$, $(^1D)3d\ ^2D$ and $(^1D)3d\ ^2S$ states are considered with the relative ratio of 1:15:8 to simulate the fast decay processes in Ar_2. Here, the intensity ratio is taken from the fitting procedure in Fig. 4(b). It can be seen in Figs. 5(a) and 5(c) that rather good agreement between experiment and calculations is achieved for the fast ICD channel in Ar_2.

For the slow ICD channel, the KER distribution is presented in Fig. 5(b), which exhibits a pronounced peak at 5.2 eV and a second peak (or an extended intensity) ranging down to 3.5 eV. Here, the decay occurs with a high probability at R near the inner turning point of the potential energy curve, see Fig. 1(c). Due to the population of the higher lying ICD initial states for this decay channel, higher ICD electron energies are observed and presented in Fig. 5(d), which shows a relatively broad distribution with a tail at the high-energy side. According to the features of KER distribution in the two-dimensional (2D) map of Fig. 4(a), we can further separate the slow ICD process into two groups at $E_{ICD}^{ini} = 41.8$ eV corresponding to the diagonal line (3) in Fig. 4(a). One group (S1) belongs to the energy region of 38.8 eV $< E_{ICD}^{ini} <$ 41.8 eV, i.e., peaks (4) and (5) in Fig. 4(b) (see also Table I). As can be seen in Fig. 5(b), the measured KER spectrum for S1 shows two peaks at roughly 3.8 and 5.2 eV with relatively higher intensity for the larger KER peak. This result is consistent with the recent measurement of photon-induced ICD in Ar_2 by Rist *et al.* in which a separate KER spectrum is obtained for the Ar-$Ar^{+*}(3p^{-2}(^1D)4d\ ^2S)$ state [20]. The other group of the slow ICD process (S2) corresponds to an energy region of 41.8 eV $< E_{ICD}^{ini} <$ 45 eV, which belongs to a series of satellite states of $Ar^{+*}(3p^{-2}nl)$ with $nl = 5d, 6d, 7d, 8d$, etc. [32,33]. The obtained KER spectrum for S2 shows a major peak at roughly 5.4 eV and an extended lower intensity down to 3.5 eV. The differences in the KER spectra between the two groups of slow ICD processes are attributed to the different lifetime and nuclear dynamics of the decay channels.

IV. CONCLUSIONS

In conclusion, we have reported on a combined experimental and theoretical study of ICD induced by electron-impact ionization ($E_0 = 90$ eV) in argon dimers. In the experiment, the kinetic energies of one emitted electron and two Ar^+ ions are measured in coincidence. The relatively higher projectile energy compared to our previous study [26] ($E_0 =$ 67 eV) allows for a better separation of predominantly fast scattered projectile and slow secondary electrons. From the measurements, we obtain the projectile energy loss spectra, the correlation diagram between the kinetic energy of ICD electron and that of the fragment ions, and moreover the energies and the populations of ICD initial states. These results allow us to identify the fast and slow ICD channels and to extract the corresponding KER and ICD electron energy distributions. The fast ICD states produce a lower KER peak at ∼3.8 eV corresponding to the decay at R_{eq}. Since these states are low in energy and their decay is nearly unaffected by nuclear dynamics, they produce a peak at ∼2 eV in the ICD electron spectrum. The measured KER and ICD electron energy spectra for the fast ICD channel are well reproduced by the *ab initio* calculations [28]. By contrast, for the slow decay channel we observe relatively higher ICD electron energies, and the KER distributions show strong influence of nuclear motion with a second strong peak appearing at KER ∼5.2 eV.

Furthermore, we showed that electron-collision-induced processes in argon dimers with projectile energy below 100 eV cause an additional enhancement of the low-energy (<10 eV) electron production. This mechanism could generally be extended to biologically relevant condensed systems. We can control the energy of emitted low-energy electrons by choosing the ICD initial states at which the decay process occurs. This result suggests that the observed decay processes may have a significant influence on the radiation damage of biological tissues.

ACKNOWLEDGMENTS

X.R. is grateful for support from DFG Project No. RE 2966/3-1. T.M. acknowledges financial support by the Research Executive Agency (REA) under the European Union's Horizon 2020 research and innovation program Grant Agreement No. 705515. K.G. gratefully acknowledges the financial help of the Deutsche Forschungsgemeinschaft (FOR 1789).

[1] K. Bartschat and M. J. Kushner, Proc. Natl. Acad. Sci. USA **113**, 7026 (2016).
[2] S. M. Pimblott and J. A. LaVerne, Radiat. Phys. Chem. **76**, 1244 (2007).
[3] M. A. Huels, B. Boudaiffa, P. Cloutier, D. Hunting, and L. Sanche, J. Am. Chem. Soc. **125**, 4467 (2003).
[4] E. Alizadeh, T. M. Orlando, and L. Sanche, Annu. Rev. Phys. Chem. **66**, 379 (2015).
[5] L. S. Cederbaum, J. Zobeley, and F. Tarantelli, Phys. Rev. Lett. **79**, 4778 (1997).
[6] S. Marburger, O. Kugeler, U. Hergenhahn, and T. Möller, Phys. Rev. Lett. **90**, 203401 (2003).
[7] T. Jahnke, A. Czasch, M. S. Schöffler, S. Schössler, A. Knapp, M. Käsz, J. Titze, C. Wimmer, K. Kreidi, R. E. Grisenti *et al.*, Phys. Rev. Lett. **93**, 163401 (2004).
[8] K. Gokhberg, P. Kolorenč, A. I. Kuleff, and L. S. Cederbaum, Nature (London) **505**, 661 (2014).
[9] F. Trinter, M. S. Schöffler, H.-K. Kim, F. P. Sturm, K. Cole, N. Neumann, A. Vredenborg, J. Williams, I. Bocharova, R. Guillemin *et al.*, Nature (London) **505**, 664 (2014).

[10] P. O'Keeffe, E. Ripani, P. Bolognesi, M. Coreno, M. Devetta, C. Callegari, M. D. Fraia, K. C. Prince, R. Richter, M. Alagia *et al.*, J. Phys. Chem. Lett. **4**, 1797 (2013).
[11] M. Kimura, H. Fukuzawa, T. Tachibana, Y. Ito, S. Mondal, M. Okunishi, M. Schöffler, J. Williams, Y. Jiang, Y. Tamenori *et al.*, J. Phys. Chem. Lett. **4**, 1838 (2013).
[12] K. Schnorr, A. Senftleben, M. Kurka, A. Rudenko, L. Foucar, G. Schmid, A. Broska, T. Pfeifer, K. Meyer, D. Anielski *et al.*, Phys. Rev. Lett. **111**, 093402 (2013).
[13] F. Trinter, J. B. Williams, M. Weller, M. Waitz, M. Pitzer, J. Voigtsberger, C. Schober, G. Kastirke, C. Müller, C. Goihl *et al.*, Phys. Rev. Lett. **111**, 093401 (2013).
[14] S. D. Stoychev, A. I. Kuleff, and L. S. Cederbaum, J. Am. Chem. Soc. **133**, 6817 (2011).
[15] U. Hergenhahn, Int. J. Radiat. Biology **88**, 871 (2012).
[16] T. Jahnke, J. Phys. B: At., Mol. Opt. Phys. **48**, 082001 (2015).
[17] T. Jahnke, H. Sann, T. Havermeier, K. Kreidi, C. Stuck, M. Meckel, M. S. Schöffler, N. Neumann, R. Wallauer, S. Voss *et al.*, Nat. Phys. **6**, 139 (2010).
[18] M. Mucke, M. Braune, S. Barth, M. Forstel, T. Lischke, V. Ulrich, T. Arion, U. Becker, A. Bradshaw, and U. Hergenhahn, Nat. Phys. **6**, 143 (2010).
[19] S. Thürmer, M. Ončák, N. Ottosson, R. Seidel, U. Hergenhahn, S. E. Bradforth, P. Slavíček, and B. Winter, Nat. Chem. **5**, 590 (2013).
[20] J. Rist, T. Miteva, B. Gaire, H. Sann, F. Trinter, M. Keiling, N. Gehrken, A. Moradmand, B. Berry, M. Zohrabi *et al.*, Chem. Phys. **482**, 185 (2017).
[21] W. Iskandar, J. Matsumoto, A. Leredde, X. Fléchard, B. Gervais, S. Guillous, D. Hennecart, A. Méry, J. Rangama, C. L. Zhou, H. Shiromaru, and A. Cassimi, Phys. Rev. Lett. **114**, 033201 (2015).
[22] H.-K. Kim, J. Titze, M. Schöffler, F. Trinter, M. Waitz, J. Voigtsberger, H. Sann, M. Meckel, C. Stuck, U. Lenz *et al.*, Proc. Natl. Acad. Sci. USA **108**, 11821 (2011).
[23] G. A. Grieves and T. M. Orlando, Phys. Rev. Lett. **107**, 016104 (2011).
[24] S. Yan, P. Zhang, X. Ma, S. Xu, B. Li, X. L. Zhu, W. T. Feng, S. F. Zhang, D. M. Zhao, R. T. Zhang *et al.*, Phys. Rev. A **88**, 042712 (2013).
[25] T. Pflüger, X. Ren, and A. Dorn, Phys. Rev. A **91**, 052701 (2015).
[26] X. Ren, E. Jabbour Al Maalouf, A. Dorn, and S. Denifl, Nat. Commun. **7**, 11093 (2016).
[27] N. Saito, Y. Morishita, I. H. Suzuki, S. D. Stoychev, A. I. Kuleff, L. S. Cederbaum, X.-J. Liu, H. Fukuzawa, G. Prümper, and K. Ueda, Chem. Phys. Lett. **441**, 16 (2007).
[28] T. Miteva, Y.-C. Chiang, P. Kolorenč, A. I. Kuleff, K. Gokhberg, and L. S. Cederbaum, J. Chem. Phys. **141**, 064307 (2014).
[29] S. D. Stoychev, A. I. Kuleff, F. Tarantelli, and L. S. Cederbaum, J. Chem. Phys. **128**, 014307 (2008).
[30] J. Ullrich, R. Moshammer, A. Dorn, R. Dörner, L. P. H. Schmidt, and H. Schmidt-Böcking, Rep. Prog. Phys. **66**, 1463 (2003).
[31] X. Ren, T. Pflüger, M. Weyland, W. Y. Baek, H. Rabus, J. Ullrich, and A. Dorn, J. Chem. Phys. **141**, 134314 (2014).
[32] M. J. Brunger, I. E. McCarthy, and E. Weigold, Phys. Rev. A **59**, 1245 (1999).
[33] A. Kikas, S. Osborne, A. Ausmees, S. Svensson, O.-P. Sairanen, and S. Aksela, J. Electron. Spectrosc. Relat. Phenom. **77**, 241 (1996).